A Parametric Study on Annular Airfoil Geometry for Collector Electrodes in Electrohydrodynamic Propulsion Systems

Tanay Apte, Varvara Karenski, Mihir Jain

5/15/2026

Tanay Apte, Varvara Karenski, Mihir Jain
Ashland, Massachusetts

Abstract

Electrohydrodynamic (EHD) thrusters generate thrust without moving parts and operate silently, which makes them promising alternatives to small-scale drone propellers. However, their low thrust density remains a major hurdle. A potential contributor to this limitation is the aerodynamic drag of the collector electrode, which acts against the generated thrust. Prior collector studies have varied the ring count and duct geometry of annular collectors, or the chord and thickness of airfoil sections in linear arrays; the airfoil cross-section of an annular collector has not been parametrically characterized. This study measures the effect of collector airfoil thickness, camber, and convergence angle on the thrust of a single-stage EHD thruster, using a custom low-friction lever and load cell apparatus with the thruster powered by a nominal 8 kV and a constant electrode gap of 25.4 mm. Overall, thrust decreased with increasing thickness, camber, and convergence angle, with a maximum decrease of 30.8% relative to the control geometry; thickness and camber effects were statistically significant after accounting for testing-session variation with a mixed-effects model. The convergence angle trend did not reach significance once session-level variation was properly modeled. Contrary to the initial hypotheses, neither camber nor convergence angle produced a thrust optimum. These results suggest that, within the tested ranges, slimmer and less cambered collector electrodes yield higher thrust, although the relative contributions of aerodynamic and electrostatic effects were not isolated.

Keywords: Electrohydrodynamic, Electroaerodynamic, EHD, EAD, Thrusters, Propulsion, Annular Airfoil, Collector

Contents

1 Introduction **4**

1.1 Context and Motivation 4

1.2 Theoretical Framework of Electrostatic and Fluid interactions 4

1.3 Literature Review 7

1.4 Research Gap 9

2 Objectives and Variables **10**

2.1 Scope and Limitations 10

2.2 Variables 10

2.3 Hypotheses 11

3 Methods **12**

3.1 Lab Setup 12

3.1.1 High Voltage Power System 12

3.1.2 Force Measurement Apparatus 13

3.1.3 Data Acquisition System 14

3.2 Electrode Fabrication 15

3.3 Experimental Procedure 15

3.4 Statistical Methods 16

3.4.1 Accounting for Testing-Day Variability 16

4 Results **17**

4.1 Thickness 17

4.2 Camber 18

4.3 Convergence Angle 20

4.4 Conclusions 21

5 Discussion **22**

5.1 Potential Aerodynamic Contributions 22

5.2 Experiment Limitations and Potential Sources of Error 23

5.3 Potential Applications and Scaling 23

5.3.1 Ozone Replenishment and HAPS 24

5.3.2 Acoustically Stealthy UAVs 24

5.3.3 Micro-Scale Robotics 24

5.4 Future Work 25

1 Introduction

1.1 Context and Motivation

EHD thrusters generate thrust by accelerating ions in an electric field and transferring momentum to neutral air molecules. EHD thrusters are enabled by a process called ionic wind, which uses high-voltage electric fields to propel ions, which then collide with neutral air molecules to transfer their momentum. Because they do not have moving parts and operate silently, EHD devices have gained popularity in applications where mechanical simplicity, reduced carbon emissions, and low acoustic signature are desirable. Despite these advantages, current EHD thrusters typically offer a low thrust density, which has limited their practical adoption Xu et al. (2018). The geometry of the collector electrode presents a challenge in both electrostatics and aerodynamics, since the profile determines the electric field distribution and the aerodynamic drag produced. Current literature has largely focused on the emitter electrode's corona discharge, yet the aerodynamic influence of the collector remains poorly characterized. This study aims to investigate whether streamlined geometric profiles improve thrust. Prior work on collector geometry has addressed either the ring count and duct proportions of annular collectors or the chord and thickness of airfoil sections in linear arrays, leaving the airfoil cross-section of an annular collector uncharacterized. A parametric study is conducted to evaluate how variations in parameters of the annular airfoil affect thrust.

1.2 Theoretical Framework of Electrostatic and Fluid interactions

The physical principles governing EHD thrust and aerodynamic resistance must be established. A qualitative conceptual framework is created to represent the net thrust of an EHD propulsion system. The net thrust of the EHD propulsion system is defined as:

$$F_{net} = F_{EHD} - F_D \tag{1}$$

Where F_{EHD} is the force associated with ion-neutral momentum transfer and F_D is the aerodynamic drag of the collector electrode

Assuming total ion-neutral momentum transfer, the EHD force generated by the thruster can be expressed as the volume integral of the electric body force over the discharge region:

$$F_{EHD} = \int_{\mathscr{V}} \rho_q E \, d\mathscr{V} \tag{2}$$

where ρ_q is the local charge density and E is the electric field at each point within the electrode gap. Assuming steady ion drift and approximating the electric field and charge density as uniform within the active discharge region, the integral reduces to

$$F_{EHD} \approx \rho_q E \int_{\mathscr{V}} d\mathscr{V} \tag{3}$$

$$F_{EHD} \approx \rho_q E \mathscr{V} \tag{4}$$

where $\mathscr{V}$ denotes the volume of the discharge region. Approximating this region as having effective cross-sectional area A and gap length d, such that $\mathscr{V} = Ad$, yields

$$F_{EHD} \approx \rho_q EAd \tag{5}$$

The ionic current is given by

$$I = \rho_q v_D A \tag{6}$$

where v_D is the ion drift velocity and A is the effective cross-sectional area of flow. Solving for charge density,

$$\rho_q = \frac{I}{v_D A} \tag{7}$$

The ion drift velocity is related to ion mobility and electric field by $v_D = \mu E$. Substituting into the charge density expression gives

$$\rho_q = \frac{I}{\mu EA} \tag{8}$$

Substituting into the thrust equation,

$$F_{EHD} = \frac{IEAd}{\mu EA} \tag{9}$$

Which simplifies to

$$F_{EHD} \approx \frac{Id}{\mu} \tag{10}$$

This expression relates thrust to the ionic current I, electrode separation d, ion mobility μ under the stated uniform-field and negligible diffusion. For corona discharge, current is modeled by the Townsend Relation as:

$$I = KV(V - V_0) \tag{11}$$

Where V is the applied voltage and V_0 is the corona onset voltage dependent on the emitter's geometry. The proportionality constant K reflects the global electrode configuration and field distribution, and is therefore dependent on both emitter and collector geometry. Since $F \propto I$, and $I \propto K$, collector geometry affects the electric field distribution.

To account for the influence of collector geometry on net performance, the EHD thrust

is combined with the aerodynamic drag force acting on the collector, modeled here using a standard drag model. For a streamlined body in incompressible flow, the drag force is:

$$F_D = \frac{1}{2}\rho_{air} v_{air}^2 C_D A_f \tag{12}$$

Where ρ_{air} is air density, v is airflow velocity, C_D is the drag coefficient of the collector, and A_f is the frontal area of the collector. v is assumed to be the average velocity of neutral molecules assuming uniform momentum transfer. The drag coefficient is dependent on the Reynolds number (Re) which depends on neutral airflow velocity. Consequently, the use of C_D in this theoretical framework is a generalized qualitative scaling law rather than a constant.

To obtain a self-consistent expression for net thrust, the induced airflow velocity must be related to the generated EHD force. Under steady conditions, thrust equals the rate of momentum imparted to the air,

$$F_{EHD} = \dot{m} v_{air} \tag{13}$$

Where $\dot{m}$ is the mass flow rate of air through the discharge region. Assuming incompressible flow and uniform velocity across an effective cross-sectional area A, the mass flow rate may be expressed as

$$\dot{m} = \rho_{air} A v_{air} \tag{14}$$

Equating this with the previously derived thrust relation gives

$$\frac{Id}{\mu} = \rho_{air} A v_{air}^2 \tag{15}$$

Solving for the induced airflow velocity,

$$v_{air} = \sqrt{\frac{Id}{\mu \rho_{air} A}} \tag{16}$$

Substituting into the drag model:

$$F_D = \frac{1}{2}\rho_{air} \left(\frac{Id}{\mu \rho_{air} A}\right) C_D A_f \tag{17}$$

Canceling ρ_{air} gives

$$F_D = \frac{1}{2}\frac{Id}{\mu A} C_D A_f \tag{18}$$

By substituting the derived expressions for ion-driven momentum transfer and the drag model for a body in a fluid stream,

$$F_{net} = \frac{Id}{\mu} - \frac{1}{2}\frac{Id}{\mu A}C_D A_f \tag{19}$$

We can factor out the common term $\frac{Id}{\mu}$ to arrive at the governing equation for the thruster:

$$F_{net} = \frac{Id}{\mu}\left(1 - \frac{C_D A_f}{2A}\right) \tag{20}$$

Where I is current, d is electrode gap, μ is ion mobility, C_D is drag coefficient of the collector electrode, A_f is frontal area of the collector electrode, and A is the cross-sectional area of momentum transfer. This equation is derived under the simplifying assumptions of uniform charge density and electric field, complete ion-neutral momentum transfer, negligible ion recombination and diffusion, constant ion mobility, and uniform airflow velocity across the effective cross-sectional area. These assumptions do not hold true in experimental testing, as momentum is lost in ion-collector collisions. Consequently, this equation is not a predictive calculation; it represents a conceptual framework to demonstrate scaling relationships qualitatively.

1.3 Literature Review

Due to the ongoing development of the field of EHD propulsion, limited research has explored the effects of collector electrode geometry on net thrust. However, investigations assessing the effects of other variables on system efficiency and thrust generation have been conducted.

Drew & Pister (2017) conducted an analysis of the geometry of wire-needle and grid electrodes within EHD thrusters, particularly the effects of electrode tip angle on current generation and plasma localization. A key finding of their study was a significant correlation ($p = 0.01$) between the number of electrode tips and the Corona Inception Voltage. Conversely, Drew and Pister observed no significant effect of emitter electrode spine height on either the inception voltage or resulting discharge current. Their research provides a foundation for the geometric optimization of EHD electrodes and concludes that electrode geometry is vital to the maximization of a system's thrust. Notably, the authors concluded that decreasing the electrode gap distance increased the thrust loss factor by approximately 30%, highlighting the nonlinear balance required between compact design and aerodynamic efficiency. The deduction by Drew and Pister that "positive corona discharge is primarily driven by geometry" serves as a key confirmation for this research. This study holds the number of emitter spikes and the electrode gap constant, allowing for a concise analysis of the varying effects of collector electrode geometry. While Drew and Pister explored the effects of voltage and grid-style electrode geometries on thrust, their analysis did not extend to cylindrical electrode configurations.

An analysis of EHD propulsion devices by Masuyama (2012) provides further insight into

the effects of electrode geometry on the performance of electrohydrodynamic (EHD) thrusters. His research supports the previously determined conclusion that an increase in system voltage yielded an increase in thrust produced. A critical observation in this work is that increasing the electrode gap distance raises the voltage threshold for thrust onset but simultaneously enhances efficiency, generating more thrust per input power. Notably, Masuyama's research reports that a thrust-to-power ratio as high as 68.43 mN/W was obtained for a thruster with an electrode gap of 21 cm. An integral claim by Masuyama states that an unexplored part of EHD propulsion that must be studied includes "how much losses are induced from neutral particles colliding with the additional surface area of electrodes."

In an investigation of EHD thrust density, Gilmore & Barrett (2015) characterized the critical relationship between wire emitter gauge and corona discharge stability. They found that sufficiently large emitter electrodes "fail to result in corona inception." This relationship implies that electrode geometry dictates system output; specifically, insufficient corona discharge inherently limits resulting thrust. While Gilmore and Barrett provide a comprehensive analysis of the emitter's role in thrust production regarding the effects of emitter electrode geometry on the thrust of EHD thrusters, their research does not explore the effects of varied collector electrode geometries.

Similarly, Calvo et al. (2022), investigated the effects of cathode geometry on EHD thruster output. Though their research involves gas-facilitated EHD propulsion, they have nonetheless introduced the crucial concept that the collector electrode's geometry holds a particular significance to the function of an EHD system as a whole. Their findings reported optimal cathode width in EHD thrusters supplied with Argon to be 12mm, as any other variation, would decrease the output thrust and the thruster efficiency. The team's experiments with xenon concluded that the optimal hollow radius was 20 mm, providing the best thrust and efficiency. While Calvo et al. experimented with variables such as hollow radius, cylindrical height, and secondary electron emission coefficient, they did not include parameters of an aerodynamically streamlined body.

Kahol et al. (2023) developed dimensionless scaling relations for wire-to-airfoil thruster configurations and experimentally varied the chord and thickness of symmetric NACA 4-digit collectors in a parallel array. They found that increasing thickness enlarges the discharge section and raises the electrical thrust, but also increases the thickness-to-chord ratio and the blockage between neighboring collectors, worsening aerodynamic performance; the combination produces a local maximum in effective (net) thrust as a function of thickness for most chords tested. For a 25 mm chord, this maximum occurred at a thickness of 6 mm (thickness-to-chord ratio ≈ 0.24). Their work establishes that collector aerodynamics are critical to EHD performance, but it was limited to symmetric airfoils in a planar array.

Hou et al. (2025) investigated annular collector configurations using sawtooth and multi-ring electrodes, varying ring count and inter-ring spacing to improve thrust density. Their work establishes that annular geometries can be structurally optimized, but treats each ring as a constant-section conductor; the cross-sectional profile of the ring itself was not varied. Nelson & Drew (2024) similarly examined ducted multi-stage thrusters, focusing on duct aspect ratio and stage count rather than section geometry. Neither study parameterizes the airfoil cross-section of the annulus, which is the variable set examined here.

1.4 Research Gap

The current literature on EHD propulsion remains weighted toward parametric characterization of the emitter electrode, particularly the influence of corona wire curvature on ionic wind velocity (Gilmore & Barrett, 2015), and toward voltage–thrust scaling laws (Masuyama, 2012). In these frameworks, the collector is treated as a passive reservoir for ion neutralization. However, Masuyama identified the losses induced by neutral particles colliding with electrode surfaces as an open question; the collector cross-section, which determines its frontal area and surface profile, is the variable examined here. Within the body of work that addresses collector geometry, prior annular studies have varied ring count, duct geometry, and multi-stage scaling.

(Hou et al., 2025; Nelson & Drew, 2024), while prior airfoil-collector studies have varied chord and thickness in linear or parallel-array configurations (Kahol et al., 2023). Prior work has not combined an axisymmetric annular ring geometry with a parametrically varied airfoil cross-section, specifically the thickness, camber, and convergence angle investigated in the present study.

This combination is not the superposition of the two configurations. In a linear or parallel-array collector, projected frontal area and the cross-sectional area available for momentum transfer are set independently, as section thickness may be varied while element spacing, and therefore through-flow area, is held constant. In an annular collector the two are geometrically coupled: increasing thickness, camber, or convergence angle might increase A_f and C_D while simultaneously reducing A, suggesting multiple terms of the drag penalty $\frac{C_D A_f}{2A}$ in the relation derived above can respond to a single geometric change. The annular geometry further introduces convergence angle, a degree of freedom with no analogue in a linear collector. The closed circumferential path also produces an axisymmetric, radially convergent field without element-to-element interaction or end effects, and the curved inner surface bounds an internal passage rather than an unbounded free stream. Scaling relations established for planar wire-to-airfoil geometries therefore cannot be assumed to transfer to the annular case, and each parameter's net effect remains an open question.

The predicted nonlinear coupling between electrostatic fields and fluid dynamics makes a simplified analytical treatment insufficient for quantitatively predicting the present system, so direct experimental characterization is required. Accordingly, this study measures the relationship between collector electrode thickness, camber, and convergence angle and the output thrust of a single-stage annular EHD thruster.

2 Objectives and Variables

2.1 Scope and Limitations

The primary objective of this study is to observe trends between annular airfoil collector geometries and the net thrust of a single-stage EHD thruster for potential future optimization. The study aims to identify geometric trends and parameter ranges that maximize thrust under fixed operating conditions; efficiency and thrust-to-power ratios are not considered. This characterization is limited to specific geometric ranges and does not claim global optimization of an ideal electrode geometry. This study is solely an analysis of observed trends and does not claim to determine the mechanisms between these trends.

Due to resource constraints, exhaust velocity, collector drag, ion current, and power consumption are not empirically measured. This study focuses on steady-state thrust, and does not aim to quantify transient thrust as the thruster is powered on. Transient thrust could not be measured due to the initial impact of the lever pushrod on the load cell.

The absolute thrust produced is of less concern than the thrust values of different tests relative to each other, as the objective is to observe trends between geometries.

2.2 Variables

Within the context of this study, the emitter electrode is ring-shaped with sawtooth spikes in order to reduce corona onset voltage and increase electric field intensity. The collector electrode, featuring a cylinder with an airfoil cross-section, is located axially downstream of the emitter. The parameters of the collector electrode geometries are varied, while the emitter-collector separation and emitter geometry are kept constant.

This investigation studies three independent geometric parameters:

- Airfoil Thickness, defined as a percentage of the chord length
- Airfoil Camber, defined as a percentage of the chord length, representing the depth of the curve of the airfoil
- Convergence Angle, defined in degrees from the central axis, representing the radial convergence of the nozzle created from the ring

Airfoil Thickness and Camber are identified using 4-series NACA Numbers. For instance, the control electrode is designated as a NACA 0024 profile, indicating 0% camber, 0% camber position, and a 24% thickness-to-chord ratio. Camber position is maintained to be 30% of the chord length for all cambered airfoils.

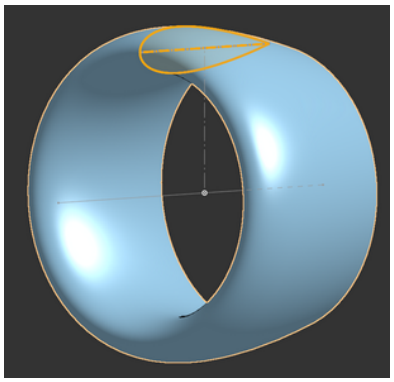

Figure 1: Control electrode: 0024, 0° convergence angle

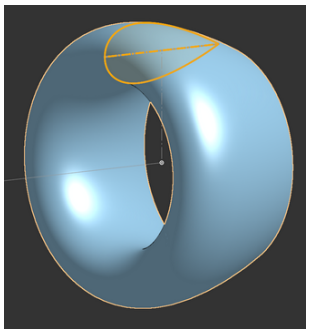

(a) Maximum thickness: 0040

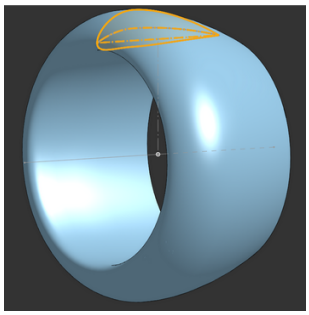

(b) Maximum camber: 8324

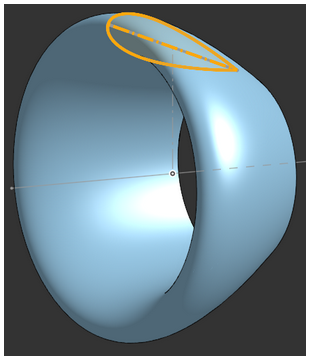

(c) Maximum convergence angle: 20°

Figure 2: Visualization of maximum collector electrode geometries

2.3 Hypotheses

Based on predicted influence of collector electrode geometry on ion collection and aerodynamic drag, the following hypotheses were formulated for each geometric parameter.

1. Airfoil Thickness: Increasing collector airfoil thickness is hypothesized to reduce net thrust over the tested range. A potential explanation is increased aerodynamic drag due to the increase in frontal area.

2. Airfoil Camber: Moderate positive airfoil camber is hypothesized to increase thrust over the tested range, while excessive camber is hypothesized to decrease thrust. A potential explanation is increased flow entrainment at moderate camber, and flow separation at excessive camber.

3. Convergence Angle: Increasing the collector convergence angle is hypothesized to increase thrust over the tested range. Thrust is hypothesized to decrease with excessive convergence angle. A potential explanation is accelerated airflow due to reduced cross-sectional area at moderate convergence angle, and increased aerodynamic drag due to increased frontal area at excessive convergence angle.

   The aerodynamic explanations proposed in the hypotheses are tentative speculations and are not proven to be the primary cause of predicted thrust trends.

3 Methods

3.1 Lab Setup

This research required the design of an experimental system in order to operate the thruster and facilitate data collection. The apparatus is comprised of three primary subsystems: a high-voltage power source, a force measurement assembly, and a data acquisition (DAQ) system.

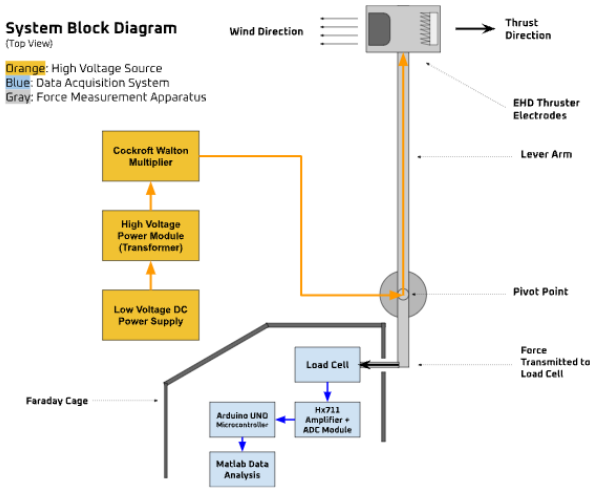

Figure 3: A block diagram of the system integration

3.1.1 High Voltage Power System

The thruster was powered by a regulated DC supply that provided a constant 10 V input. This low-voltage input was fed into a high-voltage step-up transformer module, producing an approximate intermediate potential of 3 kV. The transformer output was then connected to a Cockcroft–Walton voltage multiplier to generate the final high-voltage output of a nominal 8 kV applied to the emitter electrode. The collector electrode was maintained at ground potential.

Voltage was calculated using a high-resistance divider network and scaled according to the divider ratio. A voltage of approximately 80 volts was measured over R_2 in a voltage divider of $R_1 = 14000\text{k}\Omega$ and $R_2 = 141\text{k}\Omega$.

The applied voltage (V_{in}) was derived using the standard voltage divider relationship:

$$V_{in} = V_{out}\left(\frac{R_1 + R_2}{R_2}\right) \tag{21}$$

$$V_{in} = 80\ \text{V} \times \left(\frac{14000\ \text{k}\Omega + 141\ \text{k}\Omega}{141\ \text{k}\Omega}\right) \approx 8\ \text{kV} \tag{22}$$

The R_1 section consisted of seven 2 MΩ resistors with a 5% tolerance. The R_2 section used a 100 kΩ resistor with a 1% tolerance and a 41 kΩ resistor with a 5% tolerance. The resulting standard uncertainty in the divider ratio, and therefore in the calculated applied voltage, is approximately 1.4%, giving an applied voltage of 8.0 ± 0.1 kV.

This voltage was measured with the thruster inactive and therefore represents the multiplier output before corona onset; during operation, corona current loads the multiplier and reduces the output voltage by an amount that could not be determined without a current measurement.

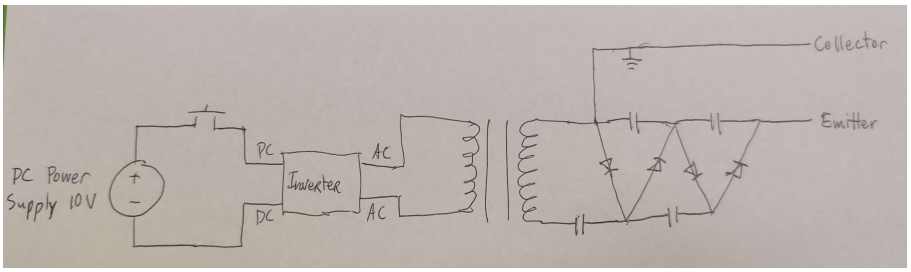

Figure 4: Circuit Diagram

3.1.2 Force Measurement Apparatus

The low-magnitude thrust generated by EHD propulsion is measured in millinewtons (mN). The force generated by the thruster was physically amplified to increase signal resolution. In order to facilitate this mechanical advantage, the experimental setup included a horizontal lever with a 6:1 ratio. The lever had one degree of freedom around a vertical yaw axis, negating the effect of gravity on the load cell's measurements. The electrodes were placed on one side, while the opposite side transferred force onto the cantilevered load cell using a rigid pushrod. During steady-state operation, the standard deviation of the thrust signal over a temporal domain was below 5 percent of the mean measured thrust, indicating reasonable measurement stability. The wires supplying voltage to the thruster were routed through an axial tube on the pivot point of the lever such that the wires would not exert a torsional force on the lever.

The lever consisted of two wooden push dowels spanning the length between the pushrod, rigid pivot point, and electrode mount. A ball bearing degreased with 98% isopropyl alcohol was used to minimize static friction along the pivot point.

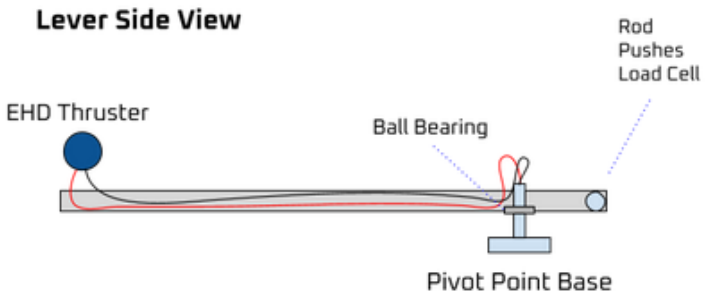

Figure 5: Lever with thruster mounted

3.1.3 Data Acquisition System

The primary components for data acquisition were a cantilevered 1 kg Wheatstone bridge load cell with a maximum electrical output of 5 mV, paired with an HX711 module, which combines a programmable-gain amplifier, set to a gain of 128, with a 24-bit analog-to-digital converter (ADC). The HX711 was connected to an Arduino UNO microcontroller board which relayed the data to MATLAB which was used to perform data processing and visualization. Amplified by the lever with a 6:1 ratio, a force of approximately 18 mN was exerted on the load cell when the thruster provided 3 mN of force, resulting in an amplified signal of 1.15 mV within the ADC. The output signal secured a signal-to-noise ratio of approximately 18 in relation to the measured noise floor of 1 mN (0.064 mV), resulting in acceptable signal resolution over the relevant measurement range of 10-40 mN. These measurements establish signal resolution but do not independently characterize load cell linearity or hysteresis.

The microcontroller was physically elevated to reduce the risk of high-voltage surface leakage or tracking along nearby surfaces. The millivolt-range wires between the load cell and the amplifier were wrapped in a grounded aluminum foil shield to prevent electrostatic charges and electromagnetic interference (EMI) from disrupting the data. A grounded Faraday cage was constructed from cardboard and aluminum foil as a continuous conductive enclosure to protect the data acquisition system from EMI from the HV generator. A star ground plane was used as a common ground reference and was connected to earth ground.

Data acquisition was automated via MATLAB and Arduino C++ scripts, triggered by a physical button input on the Arduino UNO controller. Each test cycle lasted 30 seconds and was divided into three distinct phases:

1. Baseline Calibration (0–10s): With the thruster inactive, the system recorded the average load cell output to establish a zero-reference baseline. This accounted for residual sensor offset and minor calibration errors.

2. Stabilization Period (10–20s): The thruster was activated; however, data analysis was suspended to allow the system to reach a steady state. This delay prevented measurement

inaccuracies caused by transient spikes or the initial mechanical impact of the lever arm against the load cell.

3. Thrust Measurement Phase (20–30s): The final 10 seconds of steady-state thrust were averaged.

The net thrust was determined by subtracting the initial baseline average from the final measurement average, then dividing by 6 to account for the lever ratio. For each test, standard deviation of the Thrust Measurement Phase was confirmed to be less than 5 percent of the average thrust to mitigate error from corona discharge instability. If the standard deviation was over 5 percent, the trial was discarded (no trials were discarded in this way, as they all had below 5 percent standard deviation).

3.2 Electrode Fabrication

The collector electrodes were designed as NACA 4-series airfoils, with the NACA 0024 (0 degree convergence angle) designated as the control geometry. Each collector maintained a chord length of 25.4 mm and a mid-chord diameter of 38.1 mm. The electrodes were designed using an airfoil profile generator script within the Onshape CAD software. The physical models were 3D printed in PLA and rendered conductive through the application of exactly three coats of copper-based paint. The copper paint was applied uniformly to mitigate electric field inconsistencies and upstream corona discharge from the collector's surface roughness and 3D print layers. The maximum measured resistance of each electrode was below 10 Ω. Any increase in mass caused by the coating did not affect the study, as the thruster was tested on a static lever assembly independent of gravity.

3.3 Experimental Procedure

The load cell was calibrated prior to testing using a known 50 g weight placed directly on the load cell, which was temporarily rotated 90° so that its sensing axis was aligned with gravity. This applied a force of approximately 0.49 N to the load cell and established the force conversion factor, independent of the lever. The load cell was then returned to its testing orientation, and measured forces were divided by the 6:1 lever ratio to obtain thrust. To ensure measurement accuracy before each experimental trial, the load cell output was tared to eliminate residual offset or drift from previous measurements.

Data acquisition was initiated by executing the custom MATLAB script, which established serial communication with the microcontroller and began real-time data logging and plotting of the load cell output. An initial baseline period of 10 seconds was recorded prior to energizing the high voltage supply to record steady-state baseline conditions. Following this baseline interval, the high voltage supply was activated and operated for the remainder of the programmed acquisition window.

Following each trial, raw measurement data was exported and stored in *.csv* format for subsequent analysis. The time-averaged thrust value was computed from the recorded data. After each test, the electrodes were intentionally discharged to ensure safe handling and eliminate residual electrical potential.

Testing was organized into three independent rotation sets, one for each geometric parameter. Within a set, every configuration in that sweep — including the NACA 0024 control — was tested once before any configuration was repeated, for 8 trials per electrode (9 for the convergence-angle set). The control electrode was tested within each variable's experimentation period in order to provide a baseline reference point for each variable's data. This structured rotation was implemented to mitigate the influence of thermal effects and time-dependent system drift on the comparative results. Because the three sets were run on separate days, the control geometry was re-tested within each set and yielded a different absolute mean in each. Each set was conducted over two testing sessions; trials 1-4 formed the first session and trials 5-8 (5-9 for convergence angle) the second.

3.4 Statistical Methods

The net thrust of each individual trial as described in the Data Acquisition System section is the Thrust Measurement Phase average minus the Baseline Calibration average, divided by the lever ratio. This value is referred to as raw (or total) thrust. All analyses were performed on these values. To visualize trends, thrust was graphed against collector electrode geometry's NACA number (or, respectively, convergence angle), and a trend line was fitted to the mean thrust at each geometry level. Linear regressions were used for each set, since higher powers could result in overfitting and misrepresent scaling relationships for a small parameter range. Quadratic and exponential fits were also evaluated; the quadratic term was not statistically significant for any parameter ($p = 0.38$, 0.73, and 0.53 for thickness, camber, and convergence angle), and neither alternative meaningfully improved adjusted R^2. Trend lines are descriptive; conclusions about significance rest on the ANOVA and mixed-effects analyses described below. All graphs were created using MATLAB. A one-way ANOVA on raw thrust, without accounting for testing session, is also reported for each parameter for comparison with the blocked analyses described below, with a significance threshold of $p = 0.05$.

3.4.1 Accounting for Testing-Day Variability

Testing was conducted across separate testing sessions. For each electrode geometry, tests 5-8 (tests 5-9 for convergence angle) were conducted on a different day than tests 1-4. Atmospheric conditions including ambient temperature, humidity, and barometric pressure varied between sessions and are known to influence EHD thruster performance through changes in air density and ion mobility. To quantify this effect, control electrode thrust was measured in every rotation set. Despite identical electrode geometry and nominal operating conditions, control thrust

varied by up to 34.3% across sessions (mean difference 1.08-1.46 mN, 25-34% of the overall control mean, depending on parameter), confirming that absolute thrust values are not directly comparable across testing days.

To account for this inter-session variability, thrust was analyzed using a two-way analysis of variance (ANOVA) with collector electrode geometry and testing session as fixed factors, including their interaction, and a mixed-effects model with geometry as a fixed effect and testing session as a random effect. Effect sizes (η^2) were computed for each ANOVA factor as its sum of squares divided by the total sum of squares. Where a significant interaction between testing session and geometry was identified, this was reported alongside the main effects to characterize the stability of the observed effect across sessions. As only two testing sessions were sampled per parameter, the mixed-effects variance decomposition should be interpreted as descriptive of these two sessions rather than a generalizable estimate of day-to-day variance in the experimental environment.

4 Results

4.1 Thickness

Experimental data indicated that increasing collector electrode thickness decreased net thrust, as seen in Figure 6. From electrode 0024 to electrode 0040, average thrust decreased from 3.564 mN to 3.043 mN. From electrode 0024 to 0016, average thrust increased from 3.564 mN to 4.305 mN. Statistical analysis using a one-way ANOVA yielded $p \approx 0.056$, failing to reject the null hypothesis regarding thickness and raw thrust.

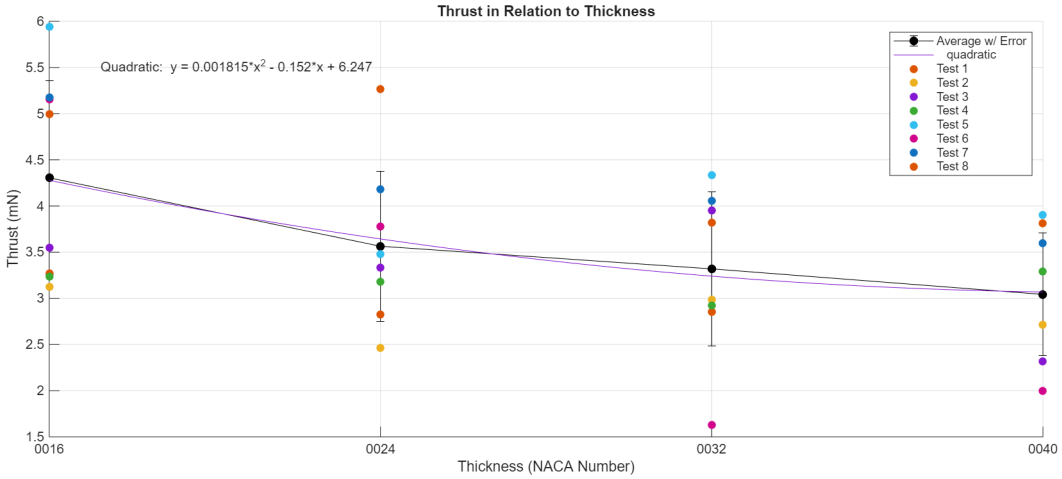

Figure 6: Total thrust vs thickness.

Points show individual trials; markers with error bars show mean ± SD at each thickness. The line is a linear fit to the level means: thrust = 4.969 - 0.0504 × thickness (% of chord) (adjusted R^2 = 0.88).

A two-way ANOVA including testing session as a blocking factor found a significant effect of thickness on raw thrust ($p = 0.0076$, $\eta^2 = 0.233$) and a comparable effect of testing session ($p = 0.0003$, $\eta^2 = 0.278$); the thickness×session interaction was not significant ($p = 0.079$), so there was no statistical evidence that the thickness effect differed between sessions, although the decline was visibly steeper in the second session (Figure 7). A mixed-effects model confirmed this result ($p = 0.0085$), attributing 47.2% of residual variance to testing session. Figure 7 shows raw thrust by thickness, split by testing session.

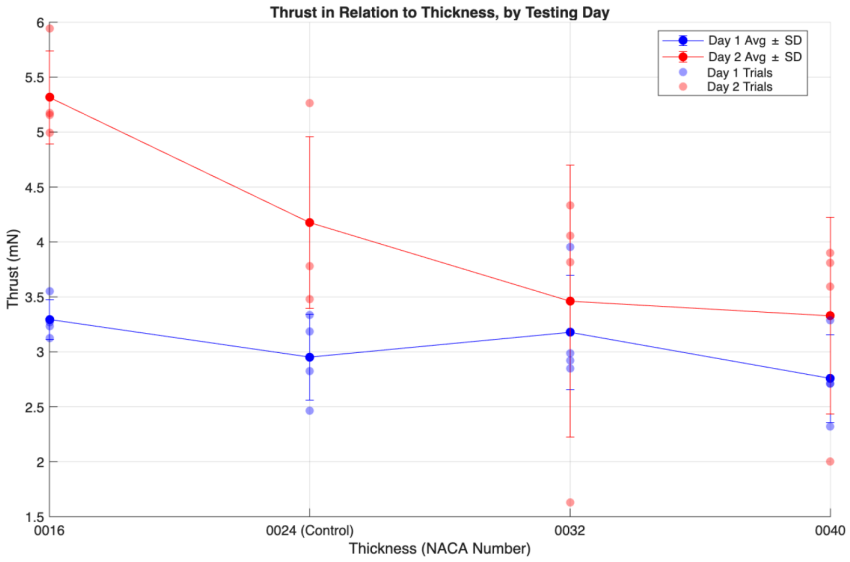

Figure 7: Raw thrust vs. thickness, split by testing session.

Points show individual trials; markers with error bars show session means ±SD. The vertical offset between sessions at every thickness level reflects the significant testing-session effect ($p = 0.0003$); both sessions trend downward with increasing thickness, reflecting the significant thickness effect ($p = 0.0076$); the difference in slope between sessions was not statistically significant ($p = 0.079$).

4.2 Camber

The experimental data indicates that the camber of the collector electrode significantly influences thrust. From electrode 0024 to electrode 8324, the average thrust decreased from ∼4.75 mN to ∼3.4 mN. An increase in camber resulted in a pronounced decrease in net thrust as seen in Figure 8, a trend confirmed by ANOVA to be highly significant ($p \approx 0.040$). Consequently, the null hypothesis regarding collector camber and total non-normalized thrust is rejected.

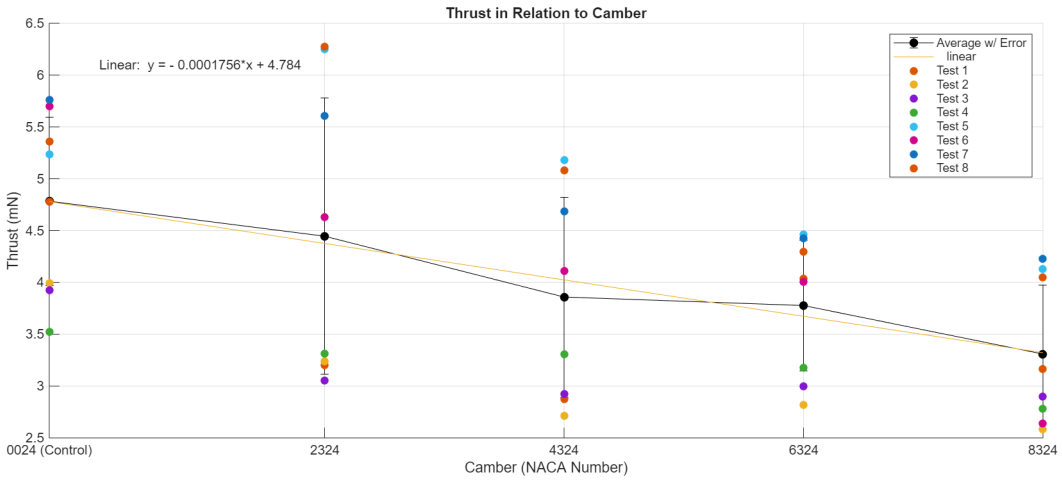

Figure 8: Total thrust vs camber.

Points show individual trials; markers with error bars show mean ± SD at each camber level. The line is a linear fit to the level means: thrust = 4.759 - 0.181 × camber (% of chord) (adjusted R^2 = 0.96). A two-way ANOVA including testing session found a significant camber effect (p = 510-6, $\eta^2 = 0.244$) and a larger effect of testing session ($p < 1 \times 10^{-6}$, $\eta^2 = 0.534$). Unlike thickness, the camber×session interaction was also significant ($p = 0.0146$, $\eta^2 = 0.073$), indicating that the magnitude of camber's effect on thrust differed between the two testing sessions (Figure 9). A mixed-effects model confirmed the camber effect persisted after accounting for session (p = 1.210-5), with testing session accounting for 80.1% of residual variance: the largest inter-session contribution of the three parameters. Because of the significant interaction, the camber effect is best reported as robust but session-dependent in magnitude, rather than a single fixed effect size.

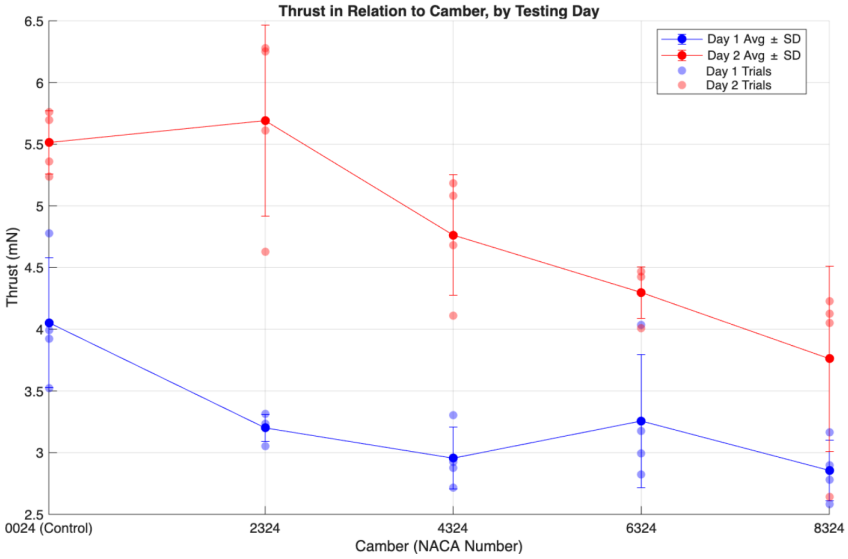

Figure 9: Raw thrust vs. camber, split by testing session.

Points show individual trials; markers with error bars show session means ± SD. Both

sessions show a declining trend with increasing camber, but the slopes differ, reflecting the significant camber×session interaction ($p = 0.0146$) — indicating the magnitude of the camber effect was not identical across the two testing sessions.

4.3 Convergence Angle

Experimental data revealed that the collector electrode's convergence angle does not significantly influence total non-normalized thrust. A one-way ANOVA refuted the statistical significance of this trend with $p \approx 0.18$, preventing the rejection of the null hypothesis. From convergence angle 0 degrees to 20 degrees, average thrust decreased from ∼4.3 mN to ∼3.5 mN. A downward trend in Figure 10 is visible, showing a slight decrease in thrust with an increase in convergence angle.

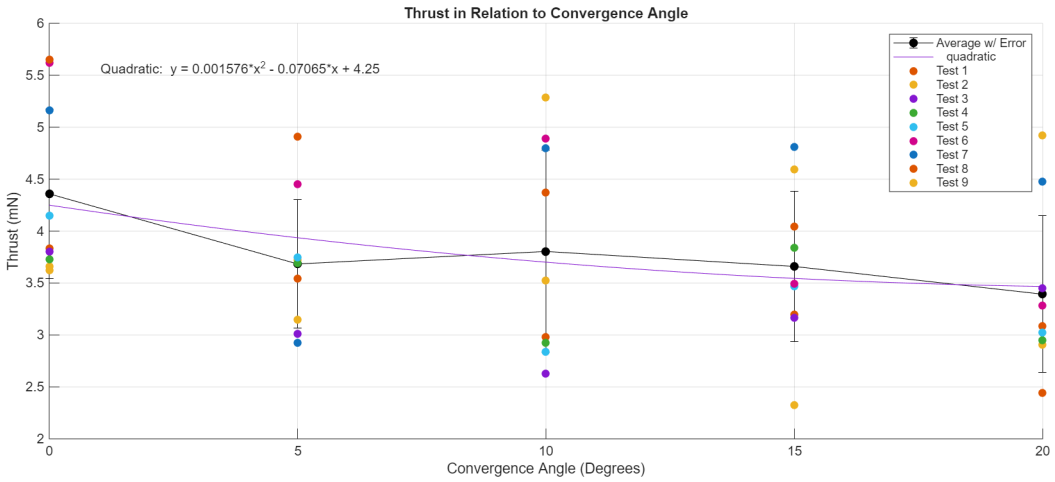

Figure 10: Total thrust vs convergence angle.

Points show individual trials; markers with error bars show mean ±SD at each angle. The line is a linear fit to the level means: thrust = 4.171 - 0.0391 × angle (degrees) (adjusted R^2 = 0.67). A two-way ANOVA including testing session found a borderline, non-significant convergence-angle effect ($p = 0.082$, $\eta^2 = 0.142$) alongside a significant session effect ($p = 0.0003$, $\eta^2 = 0.258$); the interaction term was not significant ($p = 0.521$). A mixed-effects model gave a consistent result ($p = 0.058$), just above the conventional significance threshold. Figure 11 shows raw thrust by convergence angle, split by testing session.

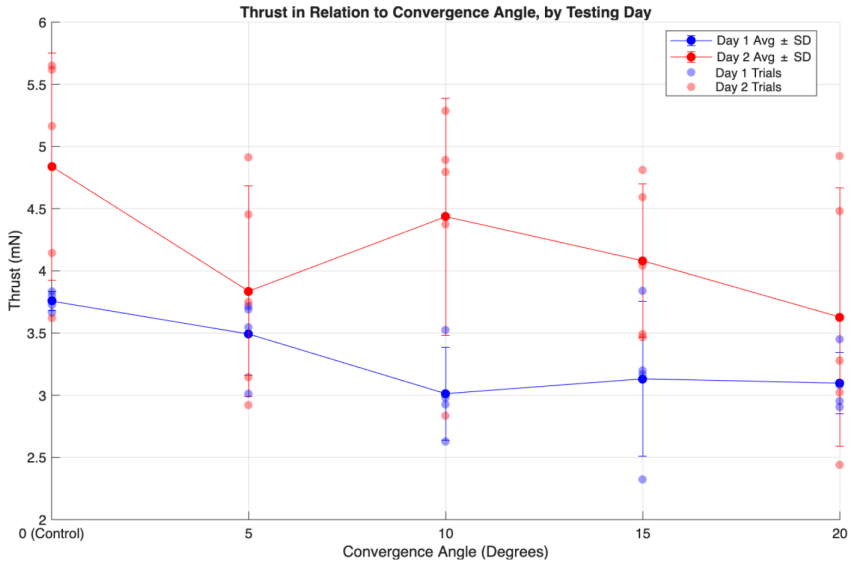

Figure 11: Raw thrust vs. convergence angle, split by testing session.

Points show individual trials; markers with error bars show session means ±SD. The consistent vertical offset between sessions reflects the significant testing-session effect ($p = 0.0003$); the modest, inconsistent change in thrust with convergence angle within each session illustrates why the convergence angle effect ($p = 0.082$) does not reach significance once session-level variation is modeled.

4.4 Conclusions

The observed decrease in thrust is consistent with a possible increase in aerodynamic resistance associated with increasing collector thickness. Experimental results contradicted the hypotheses for camber and convergence angle, with both parameters showing a negative correlation with performance. The camber trend was statistically robust to session-level blocking; the convergence-angle trend, while directionally consistent, did not reach significance once testing-session variation was properly modeled, and should be treated as suggestive rather than confirmed within this dataset. These findings suggest that for annular EHD geometries, prioritizing frontal area reduction is a primary design consideration for future optimization. In the context of the simplified governing equation derived in the theoretical framework,

$$F_{net} = \frac{Id}{\mu}\left(1 - \frac{C_D A_f}{2A}\right) \tag{23}$$

the measured decrease in net thrust with increasing thickness, camber, and convergence angle is consistent with an increase in the dimensionless drag penalty term, $\frac{C_D A_f}{2A}$, although the experiment did not measure the variables in the drag penalty term directly. Accordingly, geometrical optimization remains a primary design priority for increasing EHD thruster performance. However, a quantification of the effect of geometry on aerodynamic drag and electrostatic profile

was not available, and current was not quantified. Consequently, these trends are not explained concretely by proven aerodynamic mechanisms.

5 Discussion

5.1 Potential Aerodynamic Contributions

The drag force is proportional to the drag coefficient and frontal area, which are both dependent on collector geometry. The drag coefficient is a function of the flow's Reynolds number, which characterizes the ratio of inertial forces to viscous forces within the fluid:

$$Re = \frac{\rho_{air} v L}{\mu_{visc}} \tag{24}$$

where L is the characteristic length (in this case, the chord length of the collector, 25.4 mm), and μ_{visc} is the dynamic viscosity of air. The induced airflow velocity was not measured in this study, so it was estimated using the characteristic EHD velocity scale $u_0 = (\frac{V_a}{d})\sqrt{\frac{\varepsilon_0}{\rho}}$ defined by Kahol et al. (2023), assuming no external convection. For the nominal voltage of 8 kV and gap of 25.4 mm, this scale gives $u_0 \approx 0.85$ m/s, corresponding to $Re \approx 1{,}400$ (ρ =1.204 kg/m^3, $\mu_{visc} = 1.825 \times 10^{-5}$ Pa·s). Because u_0 is a scaling velocity and not a measured flow speed, this value is an order-of-magnitude estimate and is not a measured or validated quantity. The estimated regime is low to moderate, with laminar boundary-layer flow and a wake that may be transitional or turbulent, suggesting that frontal area may contribute substantially to drag.

Under this regime, both inertial and viscous effects contribute to aerodynamic behavior, and bluff-body drag remains strongly dependent on frontal area and characteristic length. For parallel-array wire-to-airfoil collectors, Kahol et al. (2023) found that increasing thickness raises the electrical thrust but worsens aerodynamic performance, producing a local maximum in net thrust at an intermediate thickness for most chords tested. In the present annular configuration, mean thrust was highest for the thinnest profile tested (16% thickness) and decreased across the tested range, with no optimum observed. Whether this reflects an optimum below 16% thickness or a difference between the annular and parallel-array configurations cannot be determined from the present data, since gap distance, applied voltage, emitter geometry, and collector arrangement differ between the two studies. Similarly, moderate camber was expected to entrain additional mass flow, a potential explanation drawn from ducted and free-stream flow behavior, yet mean thrust decreased across the full camber range with no observed optimum; Kahol et al. (2023) tested only symmetric airfoils, so no direct comparison is available. Increased aerodynamic drag is a plausible explanation for these trends, but because drag and electric field strength were not measured directly, it remains a candidate explanation rather than an established mechanism. Additionally, since the Reynolds number depends on both flow

velocity and characteristic length, the Reynolds number estimate would not necessarily remain constant at different scales or operating conditions.

5.2 Experiment Limitations and Potential Sources of Error

Several potential sources of systematic and environmental error may have introduced variance into the experimental results. Mechanical resistance within the ball bearing may have influenced force transmission through the lever. The precision of data acquisition may have been affected by load cell drift, in which sensor output may differ over time due to prolonged strain or internal temperature variances; this was mitigated by establishing a new baseline reference within each 30-second test window. The load cell was calibrated at a single point (50 g); linearity, hysteresis, and calibration uncertainty over the 10–40 mN measurement range were not characterized, and a multi-point calibration is a potential consideration for future work. Environmental factors also present challenges, as fluctuations in ambient humidity and temperature may alter the dielectric strength of air and the stability of the corona discharge, and inconsistent air currents within the testing facility may introduce lateral forces on the lever. Due to resource constraints, these fluctuations could not be quantified. The two-way ANOVA and mixed-effects models account for variation between testing sessions, but not for variation within a single session. Operating voltage and corona current were not measured for each geometry. Because collector geometry may alter corona current and therefore multiplier loading, geometry-dependent variation in operating voltage cannot be ruled out as a confounding variable. Coating thickness and uniformity were also not measured directly beyond electrical resistance, so variation in the copper coating between electrodes may have introduced a slight uncontrolled source of variation in the local electric field.

In addition, ion current and power consumption were not monitored, so the electrostatic contribution to net thrust could not be separated from the aerodynamic contribution. Because the drag penalty term and the current term in the governing relation both depend on collector geometry, the two cannot be distinguished from thrust measurements alone. Aerodynamic drag and exhaust velocity were similarly not measured, and the characteristic velocity underlying the stated Reynolds number is a scaling estimate rather than a measured quantity. Direct measurement of ion current and exhaust velocity would allow the contribution of each mechanism to be resolved, and is in consideration for future study.

5.3 Potential Applications and Scaling

The optimization of thrust density and power efficiency provides a potential framework for transitioning EHD technology from specialized laboratory setups to potential atmospheric propulsion systems. By eliminating the mechanical complexities and moving parts inherent in rotary

propulsion, optimized EHD thrusters offer a solid-state alternative with advantages in several thrust-critical domains.

5.3.1 Ozone Replenishment and HAPS

The utilization of optimized EHD actuators presents a potential propulsion alternative for High-Altitude Pseudo-Satellites (HAPS) operating within the lower stratosphere. At altitudes approaching 20 kilometers, the reduction in atmospheric density significantly diminishes aerodynamic drag, which partially offsets the lower thrust-to-power ratios characteristic of ionic wind generation in rarefied media. In this environment, EHD systems may provide low-magnitude thrust required for the persistent station-keeping of solar-electric gliders and lighter-than-air communication platforms. A chemical consequence of the electrical ionization of air through corona discharge is the formation of triatomic oxygen, or ozone (O_3), as a dilute byproduct. Unlike conventional chemical propulsion systems that emit nitrogen oxides (NO_x) and water vapor—compounds known to catalyze the depletion of stratospheric ozone—the EHD process yields an exhaust profile that is chemically congruent with the existing atmospheric composition. While the volumetric output of ozone from a decentralized fleet of HAPS is negligible relative to the multi-billion ton annual production cycle driven by solar photochemistry, it represents an ecological alternative to traditional aviation emissions. The deployment of EHD-driven HAPS presents a dual-purpose role where the propulsion mechanism maintains the integrity of the stratospheric chemical environment. In this framework, the generation of ozone is classified as a secondary byproduct benefit that avoids the introduction of anthropogenic pollutants, ensuring that the act of maintaining persistent telecommunications infrastructure does not compromise the protective utility of the ozone layer.

5.3.2 Acoustically Stealthy UAVs

The near-silent acoustic profile of optimized EHD systems makes them applicable to stealth Uncrewed Aerial Vehicles (UAVs) and environmental monitoring drones. Because these systems minimize the acoustic footprint by removing the broadband noise of spinning blades, they allow for covert surveillance or non-disruptive wildlife observation in noise-sensitive ecosystems. Unlike traditional battery-powered propellers, these ion-driven systems may offer a higher degree of mechanical reliability due to the total absence of rotating parts and frictional wear.

5.3.3 Micro-Scale Robotics

Furthermore, the thrust-to-weight advantages of EHD systems scale well at the micro-level. As vehicle size decreases thrust density remains constant, causing thrust to scale with the square of the characteristic length, while mass scales with the cube of the characteristic length, proportional to the volume of the vehicle. This scaling law can permit a higher thrust-to-weight

ratio in small-scale applications. This makes optimized EHD propulsion a potential candidate for insect-scale micro-robotics, where traditional electromagnetic motors are often too heavy or mechanically inefficient to sustain autonomous flight. However, as the distance between electrodes decreases, the thruster is more prone to the dielectric breakdown of air and an increased corona onset voltage. The thrust-to-power ratio of the thruster will also decrease, as more current is required to sustain constant thrust as electrode gap decreases due to Paschen's law. This suggests that the primary problem for EHD-driven micro-scale robotics is likely to be power storage.

5.4 Future Work

This study provides a preliminary dataset for a collector configuration that remains under-characterized, and suggests that frontal-area reduction is a likely geometric consideration for annular collectors within the ranges tested. Several extensions follow. Instrumenting the system to measure ion current and exhaust velocity would permit the electrostatic and aerodynamic terms to be isolated and the qualitative scaling relation derived here to be tested quantitatively. Extending the parameter sweep below the 16% thickness tested in this study would determine whether thrust continues to increase as the profile thins or whether a lower bound exists where the collector no longer supports stable ion collection. The transition from single-stage to multistage operation introduces additional fluid-structure interactions, and future experiments may investigate how the wake and ionized plume from initial stages affect the potential gradient and pressure distribution of subsequent stages.

References

Calvo, E. M., Pinheiro, M. J., & Sá, P. A. (2022). Modeling of electrohydrodynamic (ehd) plasma thrusters: Optimization of physical and geometrical parameters. *Applied Sciences*.

Drew, D. S., & Pister, K. S. J. (2017). Geometric optimization of microfabricated silicon electrodes for corona discharge-based electrohydrodynamic thrusters. *Micromachines*, *8*(5), 141. doi: 10.3390/mi8050141

Gilmore, C., & Barrett, S. (2015). Electrohydrodynamic thrust density using positive corona-induced ionic winds for in-atmosphere propulsion. *Proceedings of the Royal Society A*, *471*. doi: 10.1098/rspa.2014.0912

Hou, M., Zhang, J., & Quan, R. (2025). Sawtooth multi-ring electrodes for ionic wind propulsion. *Scientific Reports*, *15*(1), 17471. Retrieved from `https://doi.org/10.1038/s41598-025-02775-5` doi: 10.1038/s41598-025-02775-5

Kahol, O., Belan, M., Pacchiani, M., & Montenero, D. (2023). Scaling relations for the geometry of wire-to-airfoil atmospheric ionic thrusters. *Journal of Electrostatics*.

Masuyama, K. (2012). *Performance characterization of electrohydrodynamic propulsion devices* (Tech. Rep.). Massachusetts Institute of Technology.

Nelson, C. L., & Drew, D. S. (2024). High aspect ratio multi-stage ducted electroaerodynamic thrusters for micro air vehicle propulsion. *IEEE Robotics and Automation Letters*, *9*(3), 2702–2709. Retrieved from https://doi.org/10.1109/LRA.2024.3355728 doi: 10.1109/LRA.2024.3355728

Xu, H., He, Y., Strobel, K. L., Gilmore, C. K., Kelley, S. P., Hennick, C. C., ... Barrett, S. R. H. (2018). Flight of an aeroplane with solid-state propulsion. *Nature*, *563*(7732), 532–535. Retrieved from https://doi.org/10.1038/s41586-018-0707-9 doi: 10.1038/s41586-018-0707-9